

Aquaplanet Models on Eccentric Orbits – Effects of Rotation Rate on Observables

ARTHUR D. ADAMS,¹ WILLIAM R. BOOS,^{2,3} AND ERIC T. WOLF⁴¹*Department of Astronomy, Yale University, New Haven, CT 06520*²*Department of Earth and Planetary Science, University of California, Berkeley, CA 94720*³*Department of Geology and Geophysics, Yale University, New Haven, CT 06520*⁴*Laboratory for Atmospheric and Space Physics, Department of Atmospheric and Oceanic Sciences, University of Colorado, Boulder, CO 80309*

Submitted to AJ

ABSTRACT

Rotation rate is an often considered and important property in theoretical modeling of exoplanet atmospheres, but is difficult to constrain from observations even for close-in giant planets. For hypothetical temperate water-rich terrestrial planets, the rotation rate directly affects the atmospheric dynamics and by extension the surface temperature, winds, and ice cover. The time-dependent instellation of eccentric planets in particular leads to periodic responses of the atmosphere and ocean, which in principle should also be sensitive to rotation rate. These effects in turn should propagate to features in observable radiation, particularly in the infrared. We employ a widely-used Earth climate model (the Community Earth System Model, or CESM) in a simplified, uniform slab-ocean configuration, to model the atmospheric evolution of Earth-sized planets on eccentric orbits. We consider two cases of rotation rate: an Earth-like rotation period of 24 hours, and the pseudosynchronous period which generalizes the expectation of spin synchronization for eccentric orbits. We adopt the bandpasses of the Mid-Infrared Instrument for the James Webb Space Telescope as a template for the basis of developing possible wavelengths of interest for future photometry. For a telescope capable of discerning planet-star contrasts of order 10^{-8} , the ratio of contrasts in bands centered at 7.7 and 10 μm should differ by 0.2–0.3 dex between the Earth-like and pseudosynchronous cases. This approximate magnitude of difference is also seen in the ratio of bands centered at 12.8 and 25.5 μm , with a limiting planet-star contrast of order 10^{-6} . We conclude that, for two limiting cases of edge-on viewing geometry, these differences are certainly observable given significant phase photometry, and could be observable during a primary transit or secondary eclipse. Our results are not particularly sensitive to changes of the modeled ocean depth to within a factor of a few.

1. INTRODUCTION

The framework of physical processes that governs the circulation and large-scale dynamics of Earth’s atmosphere is well understood (Salmon & Held 2001; Schneider 2006). A class of 3-D models, often referred to as general circulation models (GCMs), have been developed with this framework in mind,

and allow for analysis of the effects of changing various properties of the planetary system on the evolution of the climate (e.g. O’Gorman & Schneider 2008; Wolf & Toon 2013, 2014, 2015). Such models have also been developed for other terrestrial planets in the Solar System, particularly Venus and Mars (e.g. Rossow 1983; Barnes et al. 1993, 1996; Haberle et al. 1993; Barnes & Haberle 1996; Forget et al. 1999; Lebonnois et al. 2010; Zalucha et al. 2010; Forget et al. 2013), and explore large-scale atmospheric circulation under differences in atmospheric composition, rotation rate, and surface gravity.

Beyond the Solar System, GCMs have a considerable history of adaptation to scenarios which are becoming increasingly plausible for other stellar systems. A significant series of modifications have been undertaken to accommodate unfamiliar orbital and surface conditions. Joshi et al. (1997) present an early example of a GCM applied to a hypothetical extrasolar planet, exploring the consequences of an Earth-like model on a short-period, spin-synchronous orbit around a late-type star. Following this, Merlis & Schneider (2010) used a GCM to model an *aquaplanet*, an Earth-like planet with its entire surface covered by water, to examine how the atmospheric dynamics change for tidally-locked planets orbiting M dwarfs, with an analysis of both spin-synchronous rotation and an Earth-like, 24-hour rotation period. Such works adopt the complex physics known to drive the dynamics and evolution of Earth’s atmosphere, to predict the key physical processes on these alien worlds.

In both Joshi et al. (1997) and Merlis & Schneider (2010), the authors assume a stable ocean cover for their initial conditions. The validity of this condition is studied explicitly through the definition and continual refinement of the *Habitable Zone* (HZ). The HZ defines a range of star-planet separations where a planet with an Earth-like radius, mass, and atmospheric composition and pressure could plausibly support liquid water oceans on its surface. The foundational works for our current HZ definition rely primarily on a 1-D radiative-convective climate model (Kasting et al. 1993; Kopparapu et al. 2013). These models necessarily must make some assumptions; given the one known planet supporting life, most physical conditions in these models were matched to those of Earth. However, subsequent works built on the initial conclusions for increasingly non-Earth scenarios, such as planet obliquity (Dressing et al. 2010; Linsenmeier et al. 2015; Wang et al. 2016), planet mass (Kopparapu et al. 2014), orbital eccentricity (Kane & Gelino 2012; Linsenmeier et al. 2015; Bolmont et al. 2016; Shields et al. 2016), host stellar spectral type and evolution (Shields et al. 2013, 2014; Wolf & Toon 2015), and the effect of cloud feedback (Yang et al. 2013). Taken together, we now have a wide range of theoretical predictions for the conditions governing the possible existence and persistence of liquid water oceans on terrestrial-size planets. While the purpose of this work is not to make a critique or refinement of the currently defined Habitable Zone, we introduce it here in order to start with a range of orbital configurations currently thought to be plausible for ocean-dominated planets. Our two primary parameters are the orbital eccentricity and rotation period, both of which have undergone substantial study in recent literature.

While theoretical modeling gives us a look at the potential atmospheric dynamics, any worthwhile model must make testable predictions. In our work we focus on broadband photometry, which generally offers a greater photon count over spectroscopy, and therefore is invaluable for the faint features inherent to small, warm-to-cool exoplanets. In the study of close-in giant planets (“Hot Jupiters”) in particular, many planets have been observed indirectly via transit, secondary eclipse, and in some cases substantial phase photometry, measuring the planetary flux over an entire orbit. While transit detections have substantially advanced the population of known extrasolar planets,

secondary eclipse measurements provide a complementary set of data which helps to constrain major properties of the planet’s emission. From the depth of a planet’s eclipse we can infer the temperature of the illuminated hemisphere of the planet, and can in principle give clues to the atmospheric conditions. A key instrument for observing secondary eclipses has been the Spitzer Space Telescope, in particular the near-infrared IRAC instrument (Werner et al. 2004), which has 4 photometric bands spanning 3.6–8.0 μm . In some opportune cases Spitzer was able to observe planets in some combination of these bands for entire orbits; this gives a temporal connection between the night-side observations of the transiting planet and the day-side observations of its eclipse.

Taking inspiration from these current observational techniques, we generate predictions of eclipse depths and phase photometry from our models. Global properties such as rotation and eccentricity necessarily provoke global, potentially complex dynamical responses on the surface and in the atmosphere of a planet. We explore whether an accurate and careful treatment of these complex processes allows us to broadly discern the characteristic scale of one of these global properties (rotation rate) for a hypothetically limited set of resultant observable features.

We describe our assumptions for both orbital eccentricity and planetary rotation rate, along with the relevant background, in §2. In §3 we describe the specific GCM we employ to model our planets, and how we use them to generate predictions of observable quantities. We present our results in §4, both in the internal properties of the planets and the consequent observables.

2. THEORY OF ORBITAL GEOMETRIES AND PLANETARY CONDITIONS

2.1. Eccentricity

Numerous HZ planets are known to have nonzero eccentricity (Adams & Kane 2016). While the percentage of orbital time spent in the HZ is limited from geometry, the role of atmospheric forcing and its effects on global circulation become important for eccentric planets. The role of the Lidov-Kozai mechanism (Kozai 1962; Lidov 1962) is explored in Spiegel et al. (2010). The process allows for the existence of highly eccentric Earth-sized planets with neighboring giant planets; orbital resonances between the planets and their mutual proximities are the two critical components to the mechanism’s efficiency in increasing the eccentricity.

For eccentric orbits the mean-flux approximation (MFA) fixes the time-averaged instellation over an orbit to that of a reference planet on a circular orbit. When comparing the flux with that of Earth, as a function of the stellar luminosity, star-planet separation, and eccentricity,

$$\left\langle \frac{F}{F_{\oplus}} \right\rangle = \frac{L_{\star}/L_{\odot}}{4\pi(a/a_{\oplus})^2\sqrt{1-e^2}} \quad (1)$$

where the reference values for Earth are taken to be $F_{\oplus} = 1360 \text{ W m}^{-2}$, $L_{\odot} = 3.83 \times 10^{26} \text{ W}$, and $a_{\oplus} = 1 \text{ AU}$. Williams & Pollard (2002) find that preserving the time-averaged flux is the primary factor for sustainability of surface water on a terrestrial planet. Barnes et al. (2008) take the conclusion from Williams & Pollard (2002) and use it to define the *Eccentric HZ*, or EHZ, by scaling the semimajor axis a with eccentricity according to the MFA (Equation 1).

2.2. Rotation

Very few observational constraints exist for the rotation rates of exoplanets. From tidal arguments we expect Hot Jupiters on short orbital periods to undergo spin-orbit synchronization (usually synonymous with tidal locking) on timescales shorter than the ages of the systems (Goldreich & Soter

1966; Showman & Guillot 2002). More recently, de Wit et al. (2016) and Lewis et al. (2017) have used phase curve photometry to constrain the range of possible rotation periods for the highly eccentric giant planet HD 80606 b. No observational constraints yet exist for the rotation rate of Earth-sized exoplanets.

For planets on eccentric orbits, Hut (1981) presents a limiting rotation rate using a tidal evolution argument, analogous to the synchronous limit for circular orbits. The *pseudosynchronous* rotation (PSR) period is calculated from this pseudosynchronous rate, and may be written as in units of the orbital period as

$$\frac{P_{\text{PSR}}}{P_{\text{orb}}} = \frac{(1 + 3e^2 + \frac{3}{8}e^4)(1 - e^2)^{3/2}}{1 + \frac{15}{2}e^2 + \frac{45}{8}e^4 + \frac{5}{16}e^6} \quad (2)$$

where e is the orbital eccentricity. In the circular orbit limit ($e \rightarrow 0$), the spin frequency matches the orbital frequency, with a ratio $P_{\text{PSR}}/P_{\text{orb}} \rightarrow 1$. As $e \rightarrow 1$, this ratio approaches zero. For modest eccentricities the ratio is of order unity; we consider this case of rotation rate as a characteristic “slow” rotator. For higher eccentricities the ratio decreases precipitously, but only reaches periods as short as an Earth day under the MFA for $e > 0.99$ (Figure 1). Therefore, for all eccentricities modeled in this work, we use an Earth-like rotation period as a characteristically “fast” rotator for comparison.

The rotation rate will set the extent of Hadley circulation on the planet surface. Merlis & Schneider (2010) demonstrate that for planets on circular orbits, planets with Earth-like rotation periods (“fast” rotators) will have larger latitudinal temperature and pressure contrasts away from the equator. In contrast, where the rotation is slow ($P_{\text{rot}} \sim P_{\text{orb}}$) the surface temperature should reflect the instellation, peaking at the longitude of the substellar point.

We expect that, when planets on highly non-circular orbits are considered, many of the general predictions based on the broad regimes of rotation rate for circular orbits will be extensible. In the slow limit, the pseudosynchronous rotation rate effectively “approximates” spin-orbit synchronicity (also known as tidal locking) around the time of periastron, when radiative forcing is maximal. In the fast limit, we expect that the circulation due to Coriolis forces will operate on time scales shorter than the rate of change in instellation due to the eccentric orbit.

The effect of the rotation rate on the surface temperature should also depend on the depth of the ocean mixed layer. Bolmont et al. (2016) have explored a range of eccentricities for aquaplanet models and demonstrate that increasing the thermal inertia of the oceans damps changes in the climate more efficiently. Accordingly, faster rotation in their models reduces the sensitivity of the climate to the thermal inertia of the oceans.

The surface and atmospheric conditions translate to observables. The outgoing infrared (“long-wave”) radiation (OLR) of fast rotators should in theory exhibit a wider range of spatial variation, and vary on smaller horizontal scales than the corresponding radiation from slow rotators. We discuss the expectations of observable differences arising from variation in the rotation rate in the following section.

3. CAM, CESM, AND ITS MODIFICATIONS

The National Center for Atmospheric Research (NCAR) Community Atmospheric Model (CAM) was developed as a global climate model designed for predicting and modeling the evolution of

Table 1. Orbital Properties for Pseudosynchronously Rotating Planets with Earth-like Mean Instellation

e	a	P_{orb}	P_{rot}	Peak Instellation	
		(AU)	(days)	(days)	(P_{orb})
0.3	1.024	378.35	242.98	0.642	2725
0.4	1.045	389.88	190.65	0.489	3564
0.5	1.075	406.81	145.01	0.356	4850
0.6	1.118	431.74	105.89	0.245	7000
0.7	1.183	470.11	72.30	0.154	11109
0.8	1.291	535.70	43.45	0.081	21000
0.9	1.515	680.78	18.96	0.028	61025

NOTE—Under the Mean-Flux Approximation (Equation 1), which preserves the orbit-integrated instellation with eccentricity, the semimajor axis (and, by Kepler’s Third Law, the orbital period) scale outward as eccentricity increases. The corresponding pseudosynchronous rotation period is also calculated for the given eccentricity (using Equation 2), both in units of Earth days and in units of the orbital period. The peak instellation is defined as the subsolar stellar flux at the planet surface during periastron, which is given by $F_{\oplus}/[a(1-e)]^2$. The mean insolation for a circular orbit is taken to be 1400 W m $^{-2}$. The bolded entries correspond to the scenarios explicitly modeled in this work.

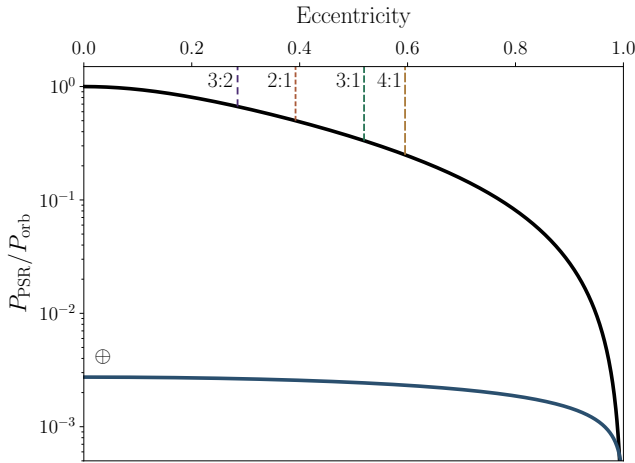


Figure 1. The theoretical pseudosynchronous rotation period matches the synchronous period (i.e. orbital period) for a circular orbit, and remains on the order of the orbital period until very high eccentricity, where the ratio (shown in black) drops precipitously as $e \rightarrow 1$. The plot assumes the orbital period scales with the Mean-Flux Approximation (Equation 1), which preserves the orbit-integrated instellation as eccentricity is changed. The ratio corresponding to a rotation period of 1 Earth day is shown as the dashed line in green. The values of eccentricity corresponding to spin-orbit resonances of 3:2 ($e = 0.285$), 2:1 ($e = 0.392$), 3:1 ($e = 0.519$), and 4:1 ($e = 0.595$) are marked.

Earth’s climate (Neale et al. 2010). CAM forms the atmospheric component of the fully coupled Community Earth System Model (CESM). The model primarily uses a *Finite Volume Dynamical Core*, described in Chapter 3 of Neale et al. (2010). The horizontal discretization uses a semi-Lagrangian flux transport scheme (Lin & Rood 1996, 1997), while the vertical discretization is termed *quasi-Lagrangian* due to a coordinate remapping. The atmospheric dynamics are computed from the primitive equations of fluid dynamics on a sphere.

The model we use in this work is an adaptation of the ExoCAM extension of CAM 4 with CESM 1.2.1. Short for Extraterrestrial CAM, ExoCAM (Wolf 2016) is designed for studies of both Earth paleoclimates and exoplanets with particular attention to expanding the valid ranges of stellar forcing, atmospheric partial pressure of greenhouse constituents (primarily CO₂ and CH₄) (Wolf & Toon 2013, 2014), and planetary rotation rate. The modifications improve the deep convection scheme to allow for moist greenhouse conditions, with mean surface temperatures $\lesssim 365$ K and water vapor partial pressures $\lesssim 0.2$ bar.

Our version of the model is closely aligned with the configuration described in Kopparapu et al. (2017). The horizontal surface resolution is $4^\circ \times 5^\circ$, and has 40 vertical levels reaching a limiting pressure of 1 mbar. We employ a commonly used “aquaplanet” configuration for simplicity: we fix the radius and surface gravity to Earth values, and have a flat topography with a uniform-depth slab ocean (Bitz et al. 2012). Ocean heat transport is neglected, but the model does account for sea ice formation, the implementation of which is the CICE model from Hunke (2008). One key difference from the aforementioned configuration is that we choose to not explicitly model cloud physics. The water ocean albedo in both the visible and near-IR is tuned to 0.3 to (crudely) account for the lack of clouds in our model; these values are much higher than those adopted with explicit cloud feedback, e.g. in Shields et al. (2013). The radiative transfer code uses the HITRAN 2012 spectral database (Kopparapu et al. 2017), using the solar spectrum. The spectral binning is divided roughly into the visible (“shortwave”) and near- to mid-infrared (“longwave”), the latter of which we describe in Table 2 to discuss the planet’s thermal emission.

3.1. Orbital Configuration

The primary divergence of our model configuration from those mentioned in the previous section comes from our changes to the orbital calculations. Our planets have highly eccentric orbits, with orbital periods dictated by the Mean-Flux Approximation (Eq. 1), and rotation periods that may differ from either the spin-synchronous or Earth-like cases.

For high orbital eccentricities, calculating the orbital position is crucial for correctly modeling the sub-stellar position and time-dependent instellation. CESM calculates the true longitude (also known as the *true anomaly* for exoplanets) of the Earth using an approximation given by a third-order polynomial by default. This approximation is valid to $\lesssim 0.3\%$ for eccentricities up to 0.1. However, the approximation rapidly diverges from the exact result, reaching $\approx 12\%$ at $e = 0.5$, and $\approx 83\%$ at $e = 0.95$. Our approach is to replace the approximation with a simple numerical method that solves Kepler’s equation,

$$M = E - e \sin E,$$

iteratively. Here E is the eccentric anomaly.

3.2. Observable Properties

Table 2. Wavelength Ranges of Model IR Spectral Bands

Band		λ_{start}	λ_{mid}	λ_{end}	Temp. Range
This Work	CAM5 ^a	(μm)		(K)	
1	2 ^b	2.50	2.76	3.08	942–1159
2	16, 1 ^b	3.08	3.42	3.84	753–942
3	15	3.84	4.02	4.20	690–753
4	14	4.20	4.37	4.55	638–690
5	13	4.55	4.67	4.81	603–638
6	12	4.81	5.15	5.56	522–603
7	11	5.56	6.10	6.76	429–522
8	10	6.76	6.97	7.19	403–429
9	9	7.19	7.78	8.47	342–403
10	8	8.47	8.77	9.09	319–342
11	7	9.09	9.62	10.20	284–319
12	6	10.20	11.11	12.20	238–284
13	5	12.20	13.16	14.29	203–238
14	4	14.29	15.04	15.87	183–203
15	3	15.87	17.70	20.00	145–183
16	2 ^c	20.00	21.62	23.53	123–145
17	2 ^c	23.53	25.81	28.57	101–123
18	1 ^c	28.57	36.36	50.00	58–101

^aSee Tables 4.6, 4.7 in the CAM5 documentation (Neale et al. 2010).

^bThese band indices are taken from the shortwave (“SW”) spectrum. All others come from the longwave (“LW”) spectrum.

^cThe ExoCAM spectrum (Wolf 2016) divides Band 2 of the LW spectral output into two separate bands. Band 1 encompasses wavelengths up to 1000 μm, but ExoCAM truncates this at 50 μm.

From pressure, temperature, and ice cover we use radiative transfer to determine the spectrum of outgoing radiation. The outgoing radiation falls into two categories: the “shortwave” (optical, near-IR) reflected light from the star, and the “longwave” (near- to mid-IR), mostly thermal radiation from the planet itself.

Thermal emission for a blackbody at temperatures characteristic of liquid water on Earth-like planets peaks at wavelengths 7.8–10.6 μm. However, this peak lies near several absorption features of water vapor, most notably a band centered at 6.3 μm. This is a broad feature that was shown to have a major dependence on rotation rate for planets receiving Earth-like instellations in Kopparapu et al. (2017) (albeit for an M-dwarf host star in that particular case); the synchronous rotation allowed much stronger moist convection at and around the sub-stellar point. Therefore we expect that the amount of water vapor in the atmosphere will largely affect how much radiation in this wavelength range escapes, relative to the expectation from purely thermal radiation. To quantify this we define the flux ratio

$$f_\lambda \equiv \frac{F_{\lambda,\text{obs.}}}{F_{\lambda,\text{therm.}}} \quad (3)$$

where λ represents some wavelength band. Here, we will compare the flux ratio within the H₂O band with that within the H₂O window. (The definition of these ranges within the model spectral output is discussed in Section 3.) This ratio of ratios, which we will call Φ , is defined as

$$\Phi \equiv \frac{f_{\text{band}}}{f_{\text{window}}}, \quad (4)$$

and should be higher where the atmosphere is drier.

An exoplanetary system can in general have any possible orientation with respect to the observer. For our analyses we restrict ourselves to 2 lines of sight for full-phase modeling, both edge-on with respect to the orbital plane: one along the periastron-star line, and another along the apoastron-star line. Such an assumption amounts to varying the argument of periastron while keeping other orientation parameters fixed. In the first case ($\omega = 90^\circ$), one would be able to observe the nightside of the planet during periastron, when the planet would transit its host star; then, one would be able to see the dayside during apoastron, when the planet passes through its secondary eclipse. In the second case ($\omega = 270^\circ$), the dayside at periastron would be visible during the eclipse, and the nightside at apoastron during transit.

To generate theoretical light curves, we take the outgoing radiation maps in each model band and calculate the expected visible flux given the geometry of the orbit relative to an observer on Earth. We use a blackbody spectrum for the model host star to then express our expected brightnesses in units of the thermal stellar flux. To compare with a realistic set of observations in the infrared, we adopt the wide filter profiles (Institute 2017) for the Mid-Infrared Imager on the James Webb Space Telescope (JWST) (Rieke et al. 2015; Wright et al. 2015; Glassey et al. 2015). These filters span a range of approximately 5–30 μm . Convolving these filter profiles with the model bands, we approximate the expected planet-star contrasts that would be observed for a JWST-like instrument. Once we have a full orbit of predicted photometry, we select the contrasts during eclipse as our predicted eclipse depths.

4. RESULTS

4.1. Internal Results

4.1.1. Conditions on the Surface

The scale of the rotation period sets contrasts in the longitudinal temperature profile. With the expectation that the spatial variation in temperature at the surface should be more latitudinal as the rotation period slows, we consider the surface temperature over the globes at the extremes of the orbits (Figure 2). The model with Earth-like rotation has a greater overall range in temperature from apoastron to periastron, with minimum and maximum values of 169.6–291.8 K, respectively. The contrast in temperature over the orbit is relatively muted in the pseudosynchronous case, where the largest contrast is now that of the day and night hemispheres. Figure 3 shows another view of the longitudinal variation in surface temperature around periastron.

The surface temperature for an ocean-covered planet directly corresponds to the sea ice cover, which drastically affects the albedo since water ice has a much higher reflectivity than liquid water. Accordingly, the spatially-resolved albedo of the planet largely mirrors the temperature distribution (Figure 4).

4.1.2. Conditions in the Atmosphere

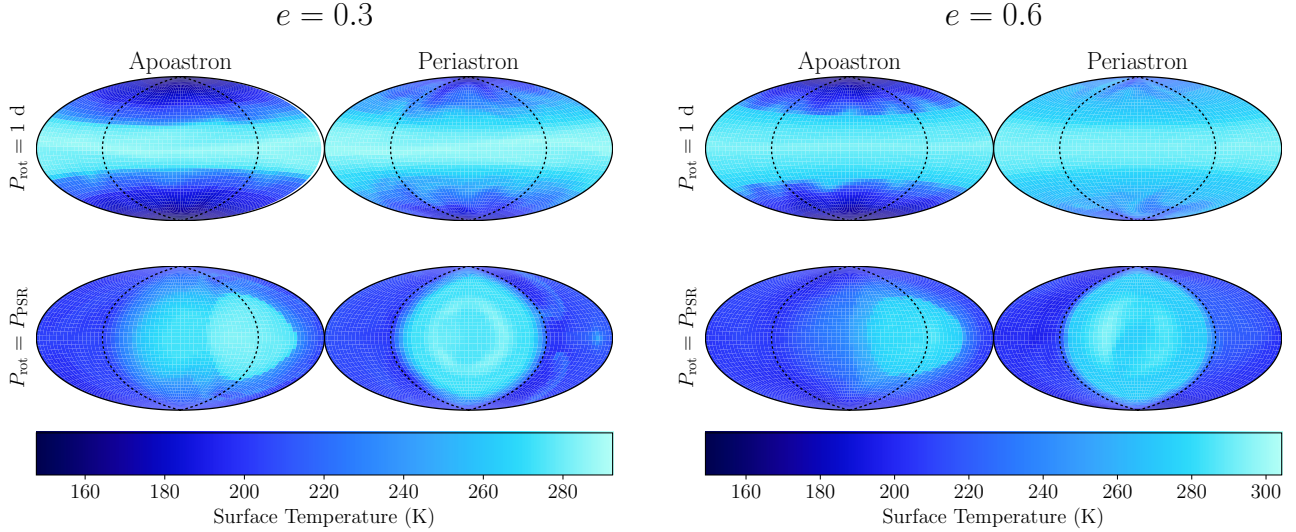


Figure 2. Global maps of the surface temperature at the extreme points of each orbit, for each of two rotation periods (Earth-like, and the pseudosynchronous period defined in Equation 2) and orbital eccentricities of 0.3 and 0.6. The dotted lines delineate the star-facing hemisphere, which is centered in each plot.

The troposphere of the slow rotator exhibits a much wider day-night difference with respect to water content (Figure 5). As we move to the upper layers of the atmosphere, the slow rotator retains a relatively elevated moisture content on both the day and night hemispheres. Considering the slowly rotating case further, we notice that the strong wet-dry difference extends to ~ 100 mbar at periastrom, compared with ~ 400 mbar at apoastrom. This reflects the larger saturation of the troposphere around the substellar point when the radiative forcing is strongest. The day-night humidity contrast seen on the slow rotator is even more pronounced at higher eccentricity, reaching to ~ 50 mbar.

Despite this strong contrast in humidity, the day-night temperature contrast in all cases is much weaker, only diverging very close to the surface for the slow rotators. The surface contrasts peak near periastrom, but persist through apoastrom for the $e = 0.3$ case. Moving to higher eccentricity means a more pronounced instellation range over the orbit, which might explain the lack of a similarly striking day-night temperature contrast during apoastrom at $e = 0.6$.

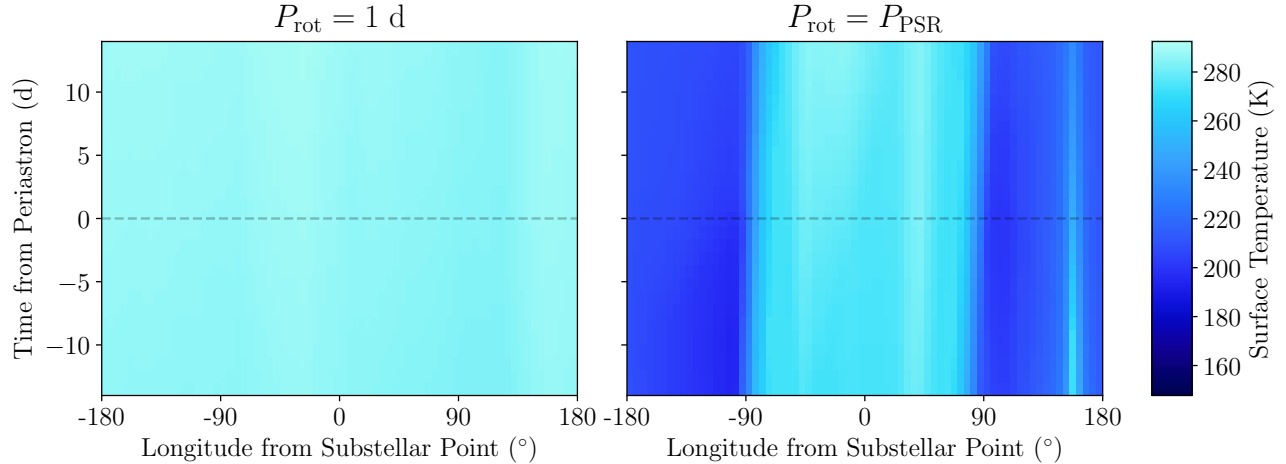
4.2. External Results

4.2.1. Outgoing Longwave Radiation

We use the OLR bins from the model to generate a low-resolution spectrum of the outgoing IR radiation (Figure 6). The peak daytime fluxes are quite similar across rotation rates and orbital phase, while the nighttime fluxes remain roughly a factor of 2 lower for the pseudosynchronous case. We can see the day-night contrast (or lack thereof) in the spatially resolved flux maps over each band (Figure 7). In the slow rotators of both eccentricities, the near- to mid-infrared bands highlight a strong day-night difference in flux.

Beyond this contrast, we also see relatively dark regions on the slow rotator day-sides that correspond to the highest column densities of water vapor in the atmosphere. Here we see more spatial information of the features seen in Figure 5. The secondary contrast, between the region of peak

$$e = 0.3$$



$$e = 0.6$$

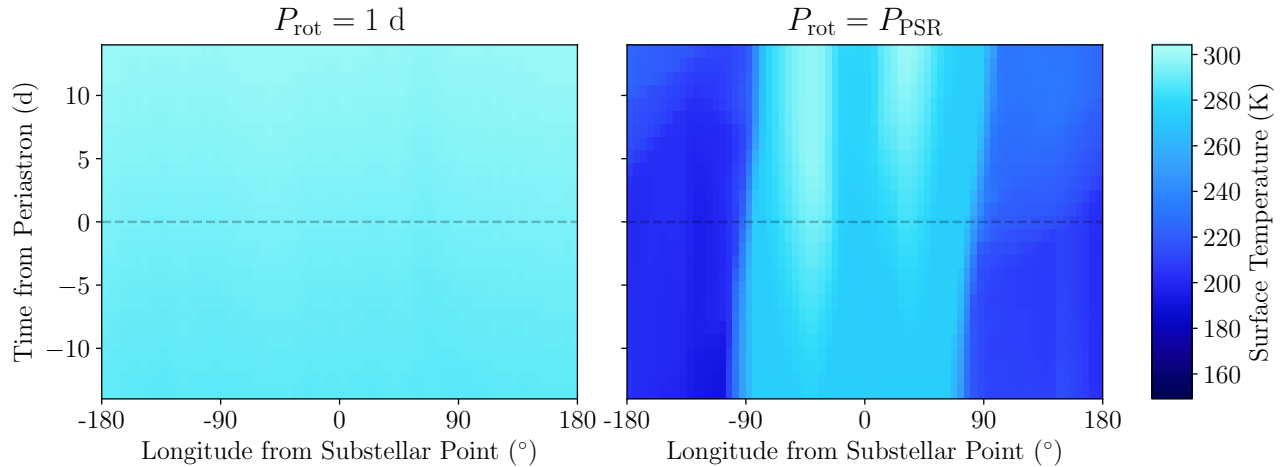


Figure 3. Surface temperatures of each rotation period and eccentricity on the planet’s equator, for the 2 weeks prior and following periastron passage. The dashed line denotes the time of periastron passage.

atmospheric saturation and the relatively drier, transparent, and bright day-side, reaches a peak starting in the band centered at $13.2 \mu\text{m}$ (Band 13 in Table 2). Returning to our definition of Φ (Equation 4), the ratio of fluxes in the parts of the IR spectrum where water molecules are least/most absorptive, we see that the contrasts with rotation rate are mirrored in the water transmission profile (Figure 8).

4.2.2. Observables

Adopting the methodology of converting model output to photometry, for the two assumed viewing geometries described in §3.2, we generate light curves for JWST-like MIRI filter profiles (Figures 9–10). We discuss two primary qualities of the resulting light curves:

1. Within each plot, we compare the broad morphology of the light curves when the rotation rate is varied. For Earth-like rotation, the variation follows the expectation of a longitudinally-

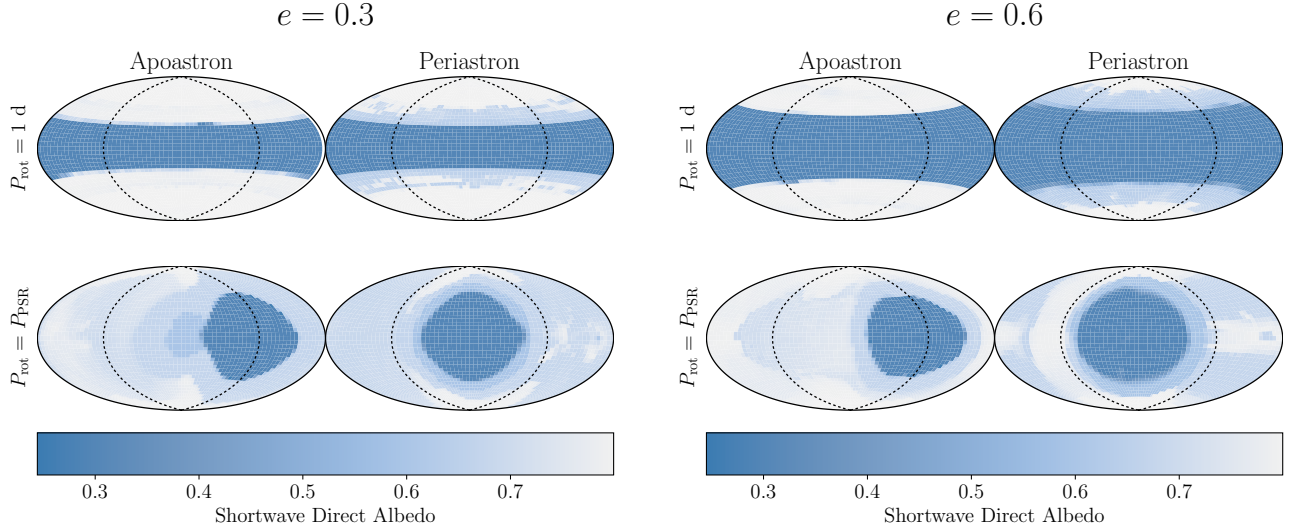


Figure 4. Global maps of the diffuse shortwave albedo at the extreme points of each orbit, for each of two rotation periods (Earth-like, and the pseudosynchronous period defined in Equation 2) and orbital eccentricities of 0.3 and 0.6. The dotted lines delineate the star-facing hemisphere, which is centered in each plot. The nominal albedo for liquid water is taken to be 0.3 (see §3 for an explanation), and the limiting albedo for thick ice cover is 0.8.

symmetric system where the flux follows the phase variations corresponding to the stellar cycle. Accordingly, these variations get a significantly higher amplitude at higher eccentricity. For the pseudo-synchronous rotation, the phase variations visibly do not follow the instellation. In particular, for $\omega = 270^\circ$, when eclipse occurs during periastron, we see the flux reach a minimum as the planet approaches periastron, directly opposing the behavior in the Earth-like case. While this is the clearest at $e = 0.3$, a dip also occurs at $e = 0.6$, although the flux immediately brightens thereafter due to the relatively faster rotation bringing the highly-irradiated hemisphere into view. At this higher eccentricity the orbit-to-orbit variations in the light curve morphologies are more pronounced, but the maximum fluxes consistently follow just after periastron passage.

2. The wavelength dependence of the light curves is more apparent for pseudo-synchronous rotation. In particular, we see both a convergence of the fluxes between the two rotation rates following periastron as we move to redder bands. Additionally, the F770W band (centered at $7.7 \mu\text{m}$) has a qualitatively different shape due to the unique transmission properties of water vapor in the atmosphere.

With these features in mind, we construct “colors” by comparing the differences of fluxes between two bands. Here we choose two pairs of bands: the bands at 7.7 and $10.0 \mu\text{m}$, and the bands at 12.8 and $25.5 \mu\text{m}$ (Figures 11–12). The first pair of bands aims to make a similar ratio as Φ (Equation 4), by comparing a band where water has a strong absorption feature with one where it is absent. The second is chosen to reflect the increase in the pseudo-synchronous light curves with wavelength, with two bands that are sufficiently different in wavelength but not extremely different in the scale of phase variations.

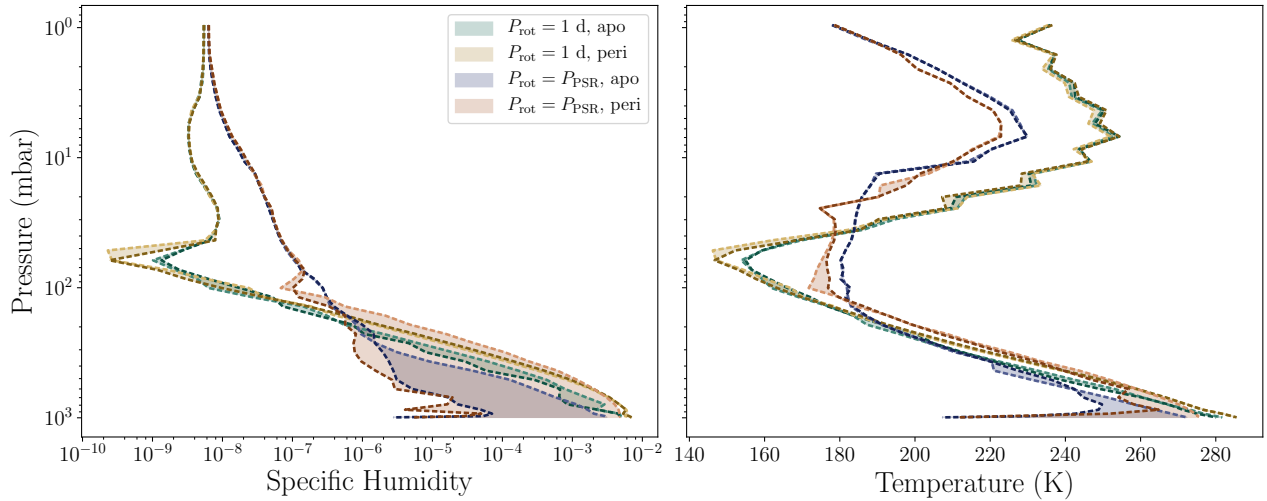
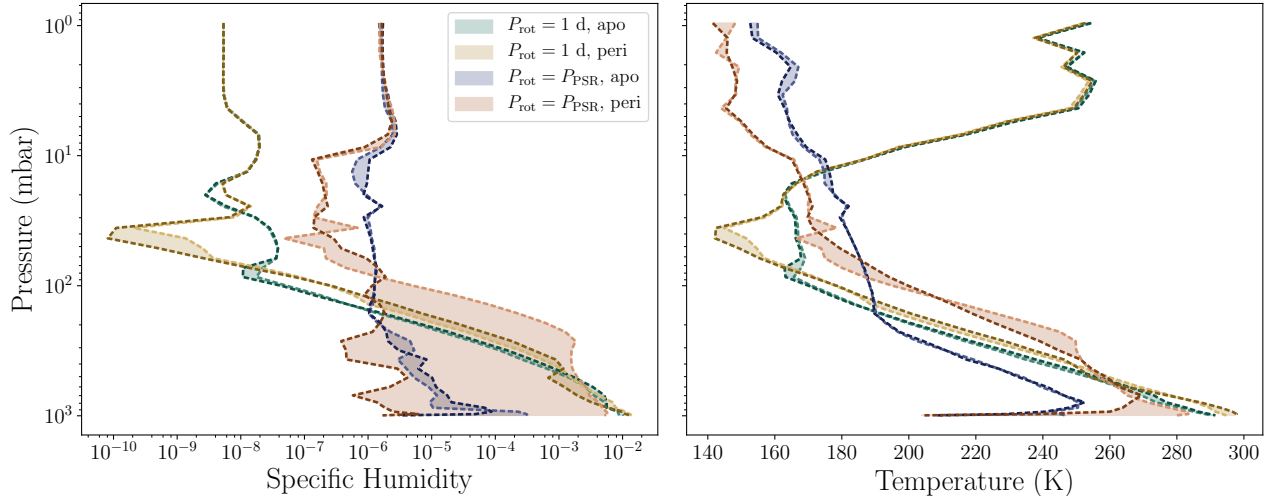
$e = 0.3$

 $e = 0.6$


Figure 5. The specific humidity (H_2O fraction of atmospheric mass) and temperature, both for atmospheric columns centered on the sub- and anti-stellar points. The lighter bounding lines represent the quantity at the substellar point, and the darker line that of the antistellar point. The colors represent the extreme points in the orbit for each of the two rotation periods.

For an eclipse-periastron viewing angle ($\omega = 270^\circ$) we see a consistent difference in the colors during or near periastron. The differences can be as high as 0.35 dex for both eccentricities. At $\omega = 90^\circ$, the differences are not well-aligned with periastron for $e = 0.3$, but do reach a maximum around quadrature. At $e = 0.6$, the pseudo-synchronous rotation period is short enough to allow a spike near periastron. The $e = 0.6$ color curves exhibit fairly significant variations from orbit to orbit, but one persistent feature is the set of secondary dips/peaks (depending on color), which correspond to the spin-orbit ratio.

Despite limiting our analysis of full-orbit photometry to two extreme cases of $\omega = 90^\circ$ and 270° , it is relatively straightforward to predict the eclipse depths for the entire range of possible observing

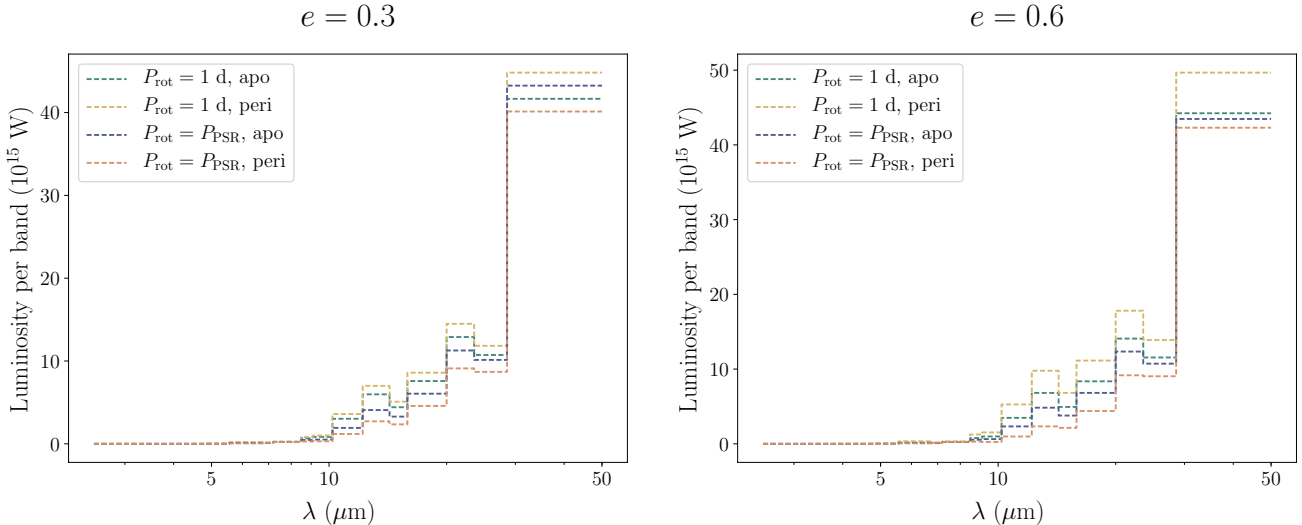


Figure 6. Spectrum of the outgoing longwave radiation (OLR) at the top of the atmosphere. The wavelength ranges for the ExoCAM bands are specified in Table 2. The colors represent the extreme points in the orbit for each of the two rotation periods.

longitudes (Figure 13). The variations in eclipse depths with viewing geometry show a similar qualitative behavior as the phase curves with respect to rotation: the fast rotators exhibit a much weaker dependence on the observing angle than the pseudosynchronous cases. This further suggests that, while maximizing the observing time would maximize the ability to discern between these cases, for a wide range of viewing geometries a pair of eclipse depths could hint at the broad timescale of rotation.

4.3. Effects of Ocean Mixed Layer Depth

The previous analysis assumed a uniform ocean depth of 50 meters. We expect that, since the observable metrics we have constructed rely on absorption characteristics of water, the depth can readily affect both the quantity and temperature of precipitable water. To explore the broad effect of the depth on our results, we re-run the $e = 0.3$ cases with ocean mixed layers depths of 10 meters. The ice cover increases slightly relative to the 50 meter case at both extremes of the orbit, for both rotation periods (Figure 14). For Earth-like rotation, the minimum latitude with ice cover is closer to the equator near apoastron, and a thinner ice cover persists where open oceans exist in the 50 meter case at periastron. With pseudo-synchronous rotation, the area of the ice-free regions are both smaller, indicating that the relatively greater susceptibility of the ocean to freeze over at shallower depths is a stronger effect than the correspondingly lower thermal inertia that would allow the ice to melt as the planet swings toward periastron.

The simulated MIRI light curves do not change appreciably in the magnitudes of planet-star contrast. The Earth-rotation curves do exhibit stronger amplitudes of phase variations compared with their deeper ocean counterparts, but this variation is still small compared with the average difference between rotation cases at fixed depth (Figures 19–21). From this we conclude that while the ocean depth has some effect on the observables, both the quality and quantity of differences are not significant enough to affect our results.

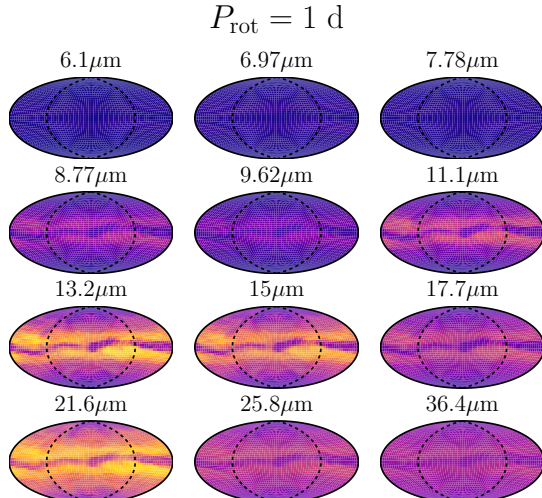
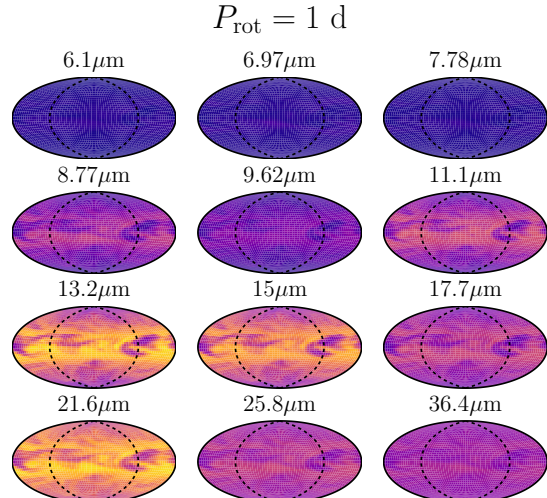
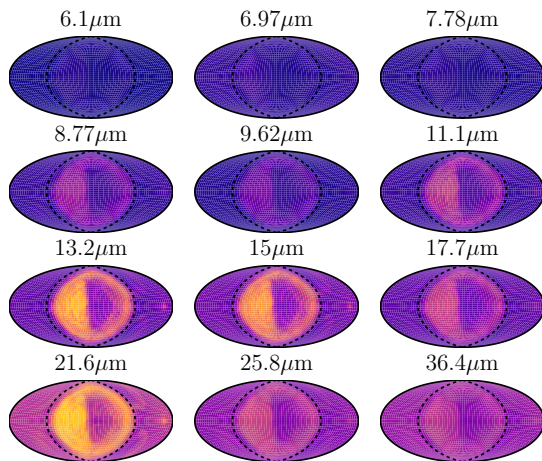
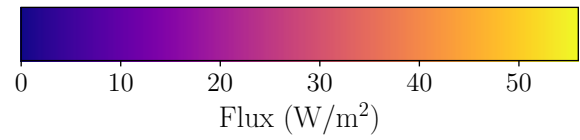
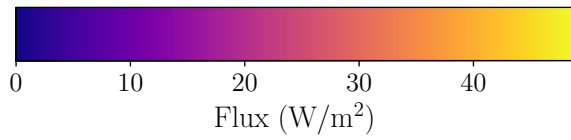
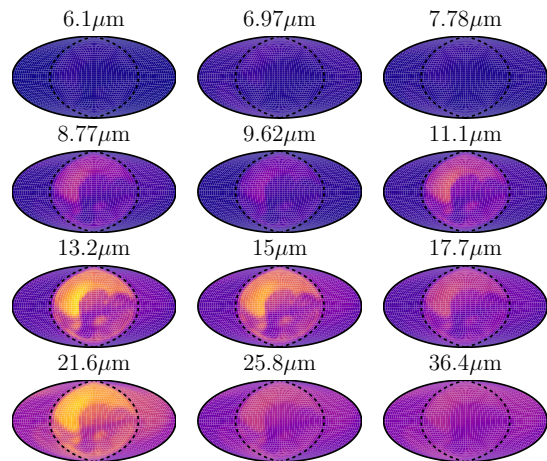
$e = 0.3$

 $e = 0.6$

 $P_{\text{rot}} = P_{\text{PSR}}$

 $P_{\text{rot}} = P_{\text{PSR}}$


Figure 7. Global outgoing flux at the top of the atmosphere for a range of infrared bands from the ExoCAM model (Bands 7–18 in Table 2), for each of the two rotation periods and orbital eccentricities. The dotted lines delineate the star-facing hemisphere, which is centered in each plot.

5. DISCUSSION

We show that, for a GCM modified to model a flat-topography ocean planet, differences in the scale of rotation rate between two physically-motivated values could be discernable from mid-infrared phase photometry of sufficient signal-to-noise. We explicitly model two contrasting viewing geometries and demonstrate that differences of order $\sim 0.3\text{--}0.4$ dex in photometric contrast ratios would be apparent

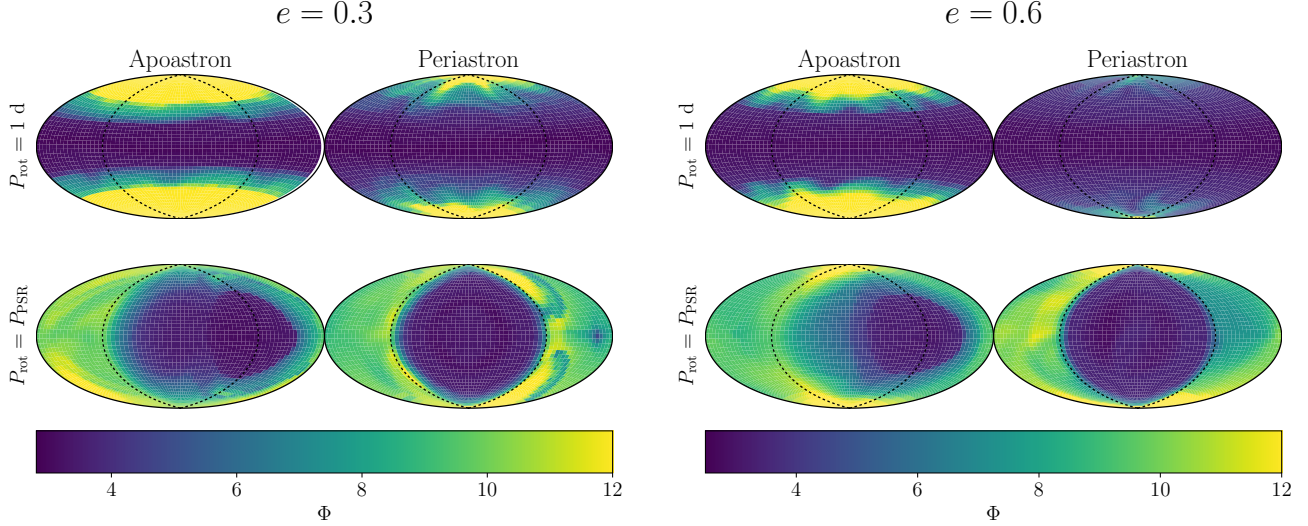


Figure 8. Global views of the H₂O band/window ratio (defined as Φ in Equation 4) at the extreme points of each orbit, for each of two rotation periods (Earth-like, and the pseudosynchronous period defined in Equation 2) and orbital eccentricities of 0.3 and 0.6. The dotted lines delineate the star-facing hemisphere, which is centered in each plot. Φ exhibits a much stronger longitudinal variation in the slowly rotating case than in the Earth-rotation case. In the Earth-rotation case, the latitudinal variation is slightly more pronounced, but the variation is smaller than the day-night side variation on the slowly rotating planet.

with just eclipse depths. These differences propagate from the differences in the spatial distribution and time evolution of atmospheric moisture content, as well as surface temperature and ice cover, influenced by the rotation.

While we have attempted to explore a constrained problem with as few added assumptions as possible, we acknowledge that we have not considered other dynamical and atmospheric effects that might otherwise contribute observables with an amplitude comparable to our phase variations. In particular, we do not take into account the effects of tidal heating/dissipation, which could induce an additional forcing term to our systems. Additionally, we have restricted ourselves to studying systems with zero spin obliquity and solar-type host stars. In a future work we will examine how these results vary for a variety of conditions for temperate terrestrial exoplanets.

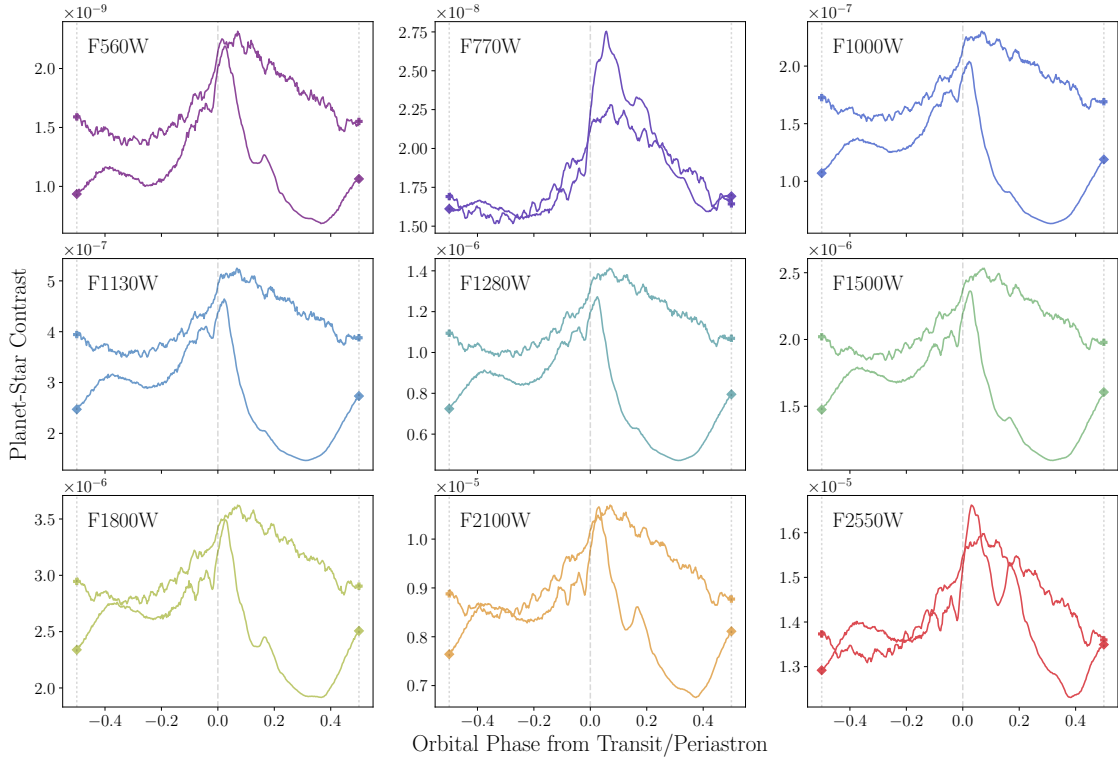
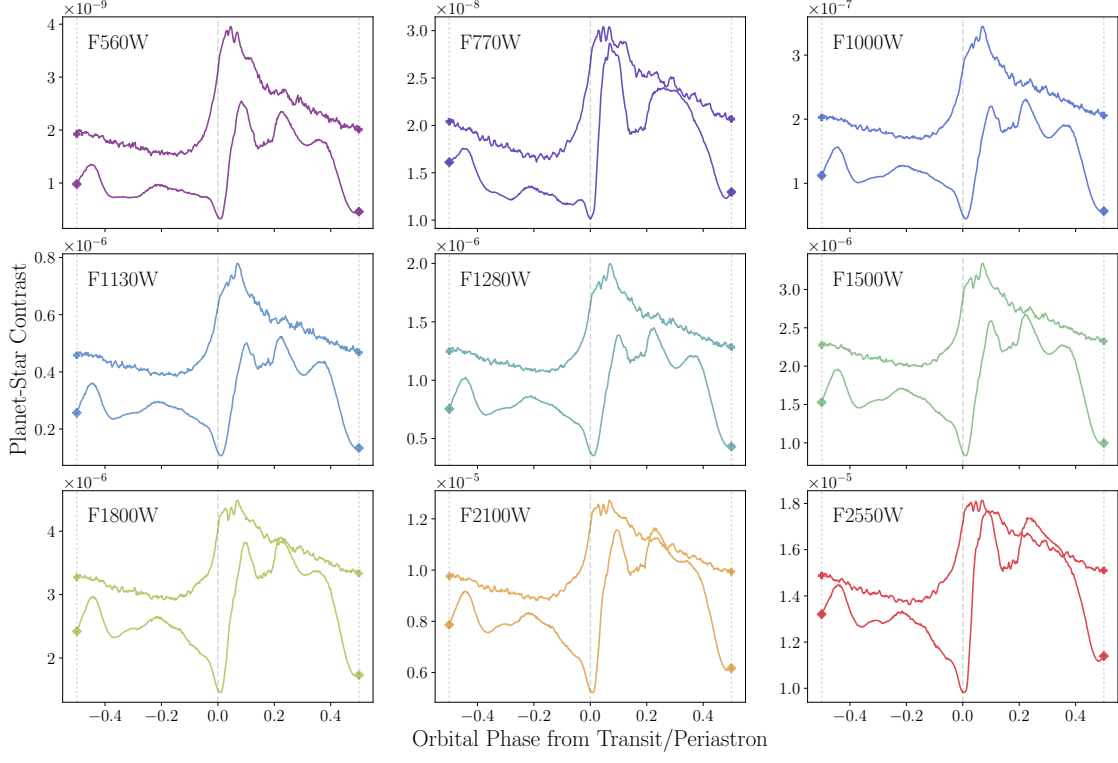
$e = 0.3, \omega = 90^\circ$

 $e = 0.6, \omega = 90^\circ$


Figure 9. Simulated light curves for a viewing geometry such that the orbit is seen edge-on, and the planet transits during periastron. Each 3x3 grid represents one of the two orbital eccentricities. The light curves are plotted for each of the 9 MIRI bands found on the upcoming James Webb Space Telescope. Within each plot, the light curve with plus-sign endpoints is for Earth-like rotation, and the curve with diamond endpoints is for pseudo-synchronous rotation.

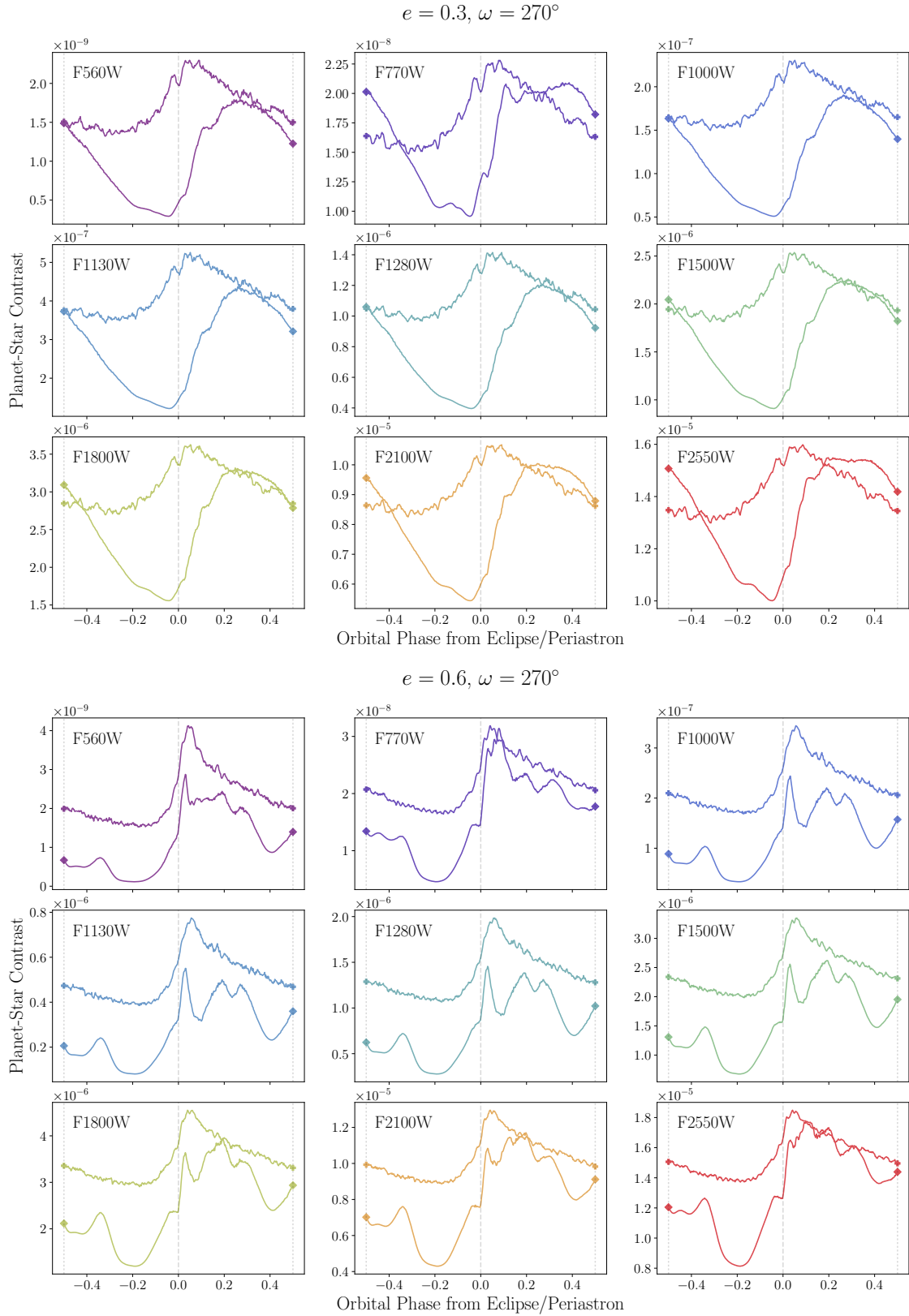


Figure 10. Simulated light curves for a viewing geometry such that the orbit is seen edge-on, and the planet undergoes secondary eclipse during periastron. Each 3x3 grid represents one of the two orbital eccentricities. The light curves are plotted for each of the 9 MIRI bands found on the upcoming James Webb Space Telescope. Within each plot, the light curve with plus-sign endpoints is for Earth-like rotation, and the curve with diamond endpoints is for pseudo-synchronous rotation.

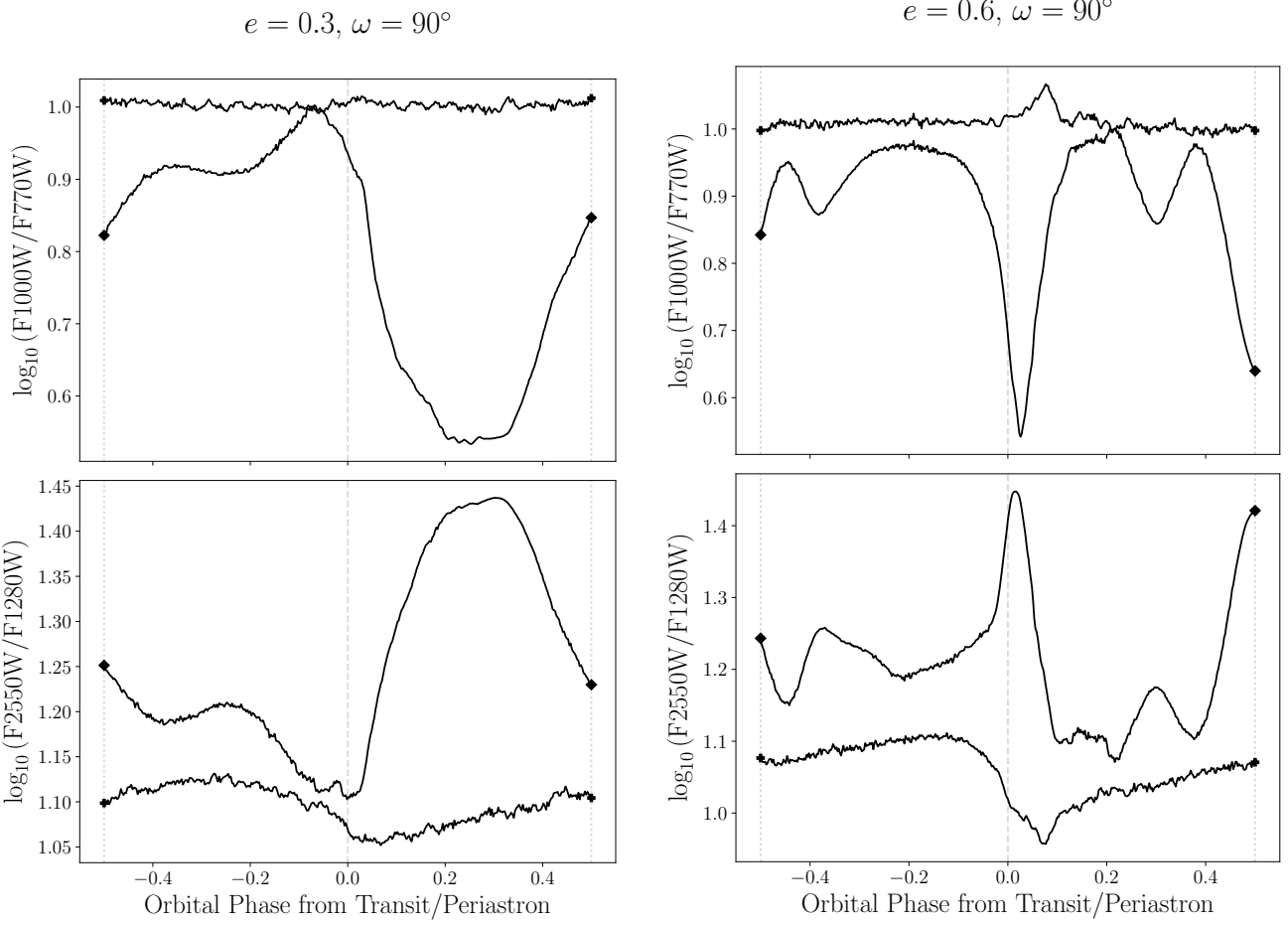


Figure 11. Ratios of a selection of the planet-star contrasts shown in the light curves of Figure 9, where the planet transits during periastron. Within each plot, the light curve with plus-sign endpoints is for Earth-like rotation, and the curve with diamond endpoints is for pseudo-synchronous rotation.

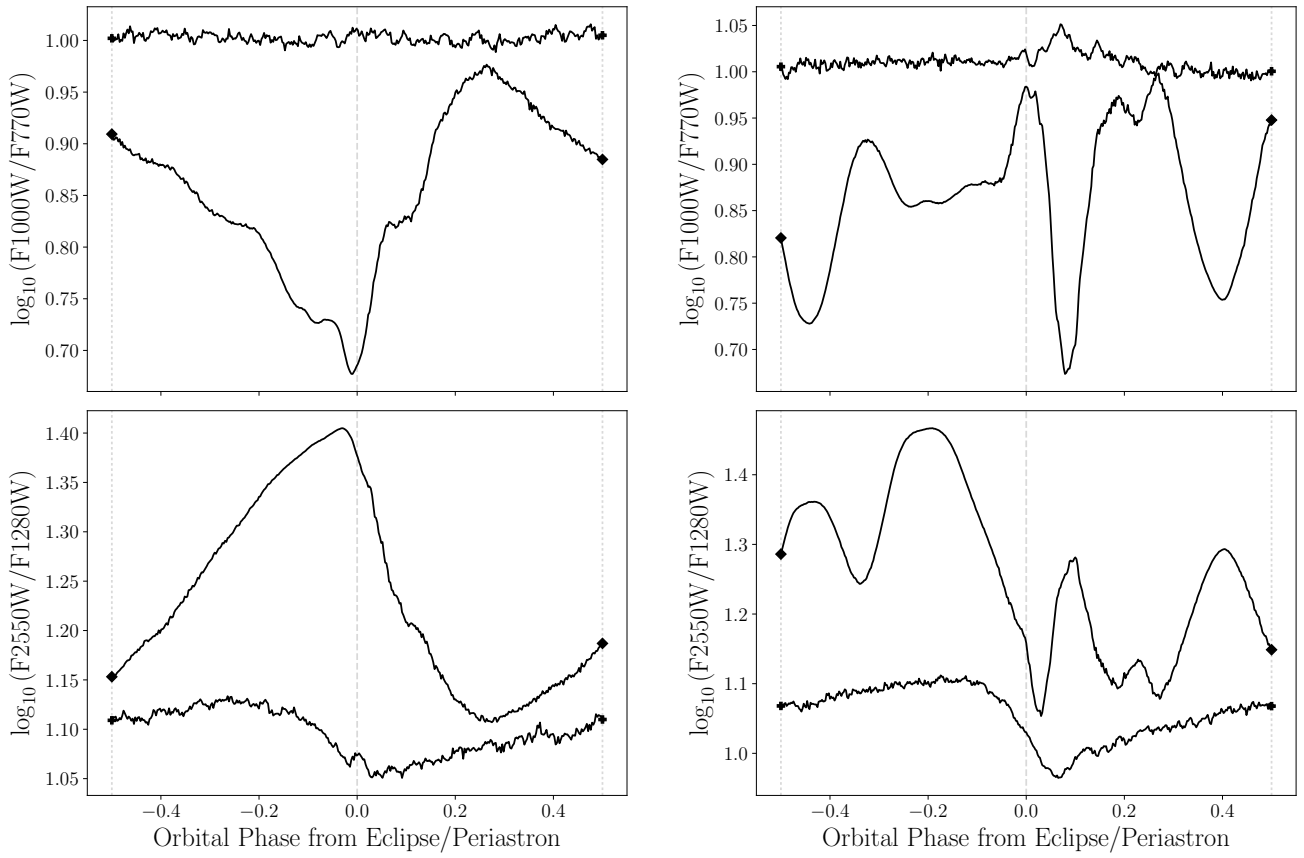
$e = 0.3, \omega = 270^\circ$ $e = 0.6, \omega = 270^\circ$ 

Figure 12. Ratios of a selection of the planet-star contrasts shown in the light curves of Figure 10, where the planet undergoes secondary eclipse during periastron. Within each plot, the light curve with plus-sign endpoints is for Earth-like rotation, and the curve with diamond endpoints is for pseudo-synchronous rotation.

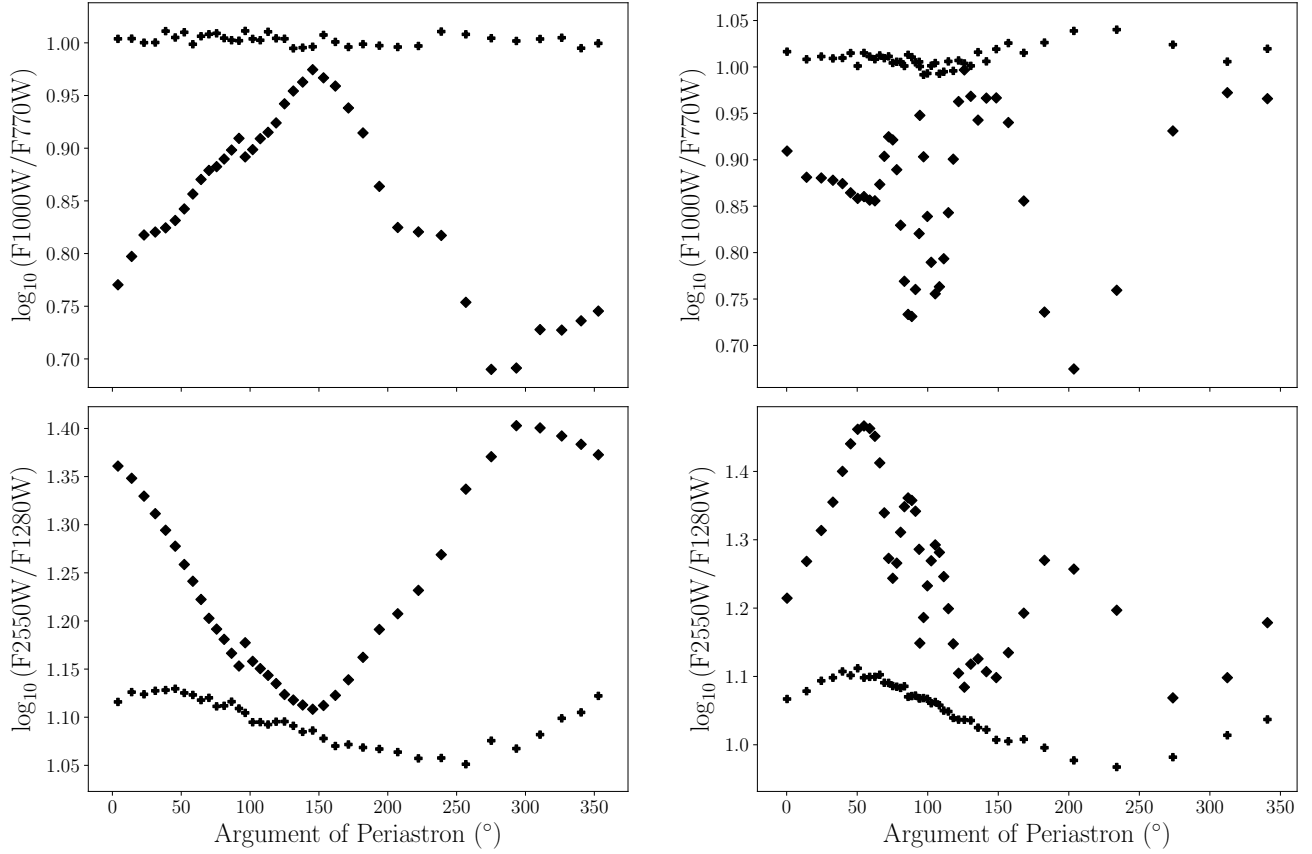
$e = 0.3$ $e = 0.6$ 

Figure 13. Predicted eclipse depth ratios for the range of possible arguments of periastron relative to an observer. The quantities are identical to those in Figures 11–12

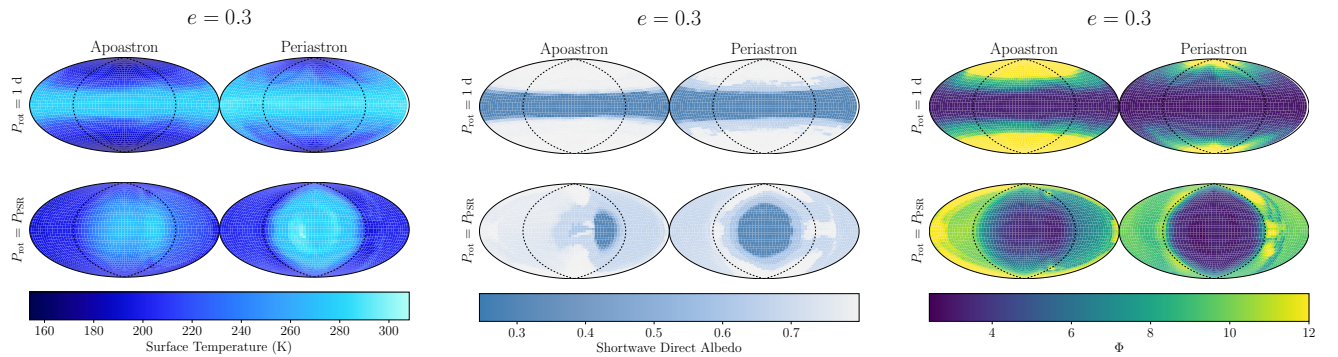


Figure 14. Same as Figures 2, 4, and 8 for ocean depths of 10 meters, for $e = 0.3$.

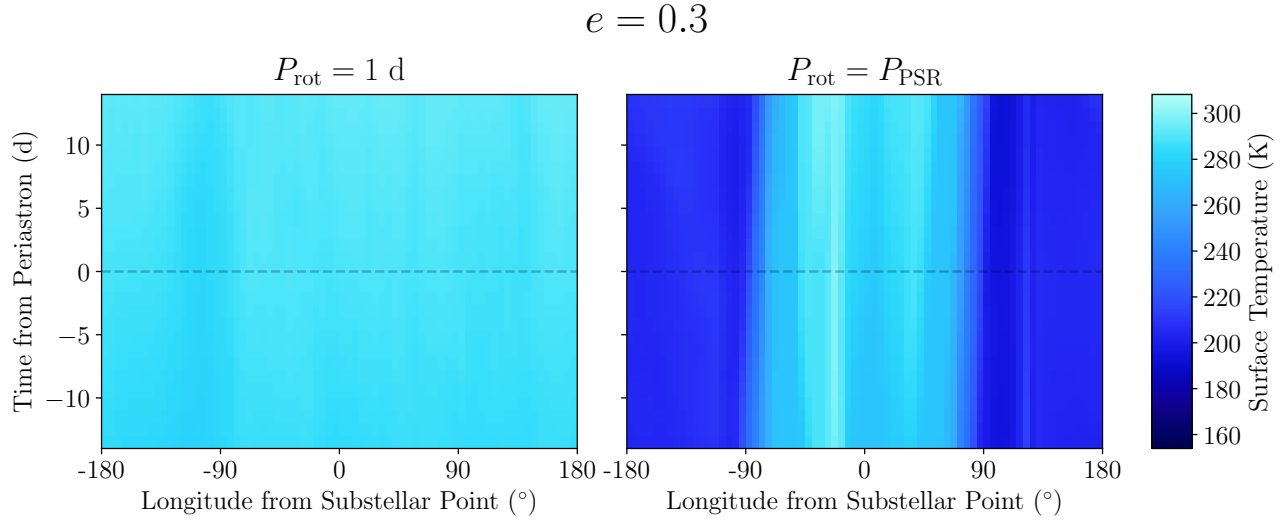


Figure 15. Same as Figure 3 for ocean depths of 10 meters, for $e = 0.3$.

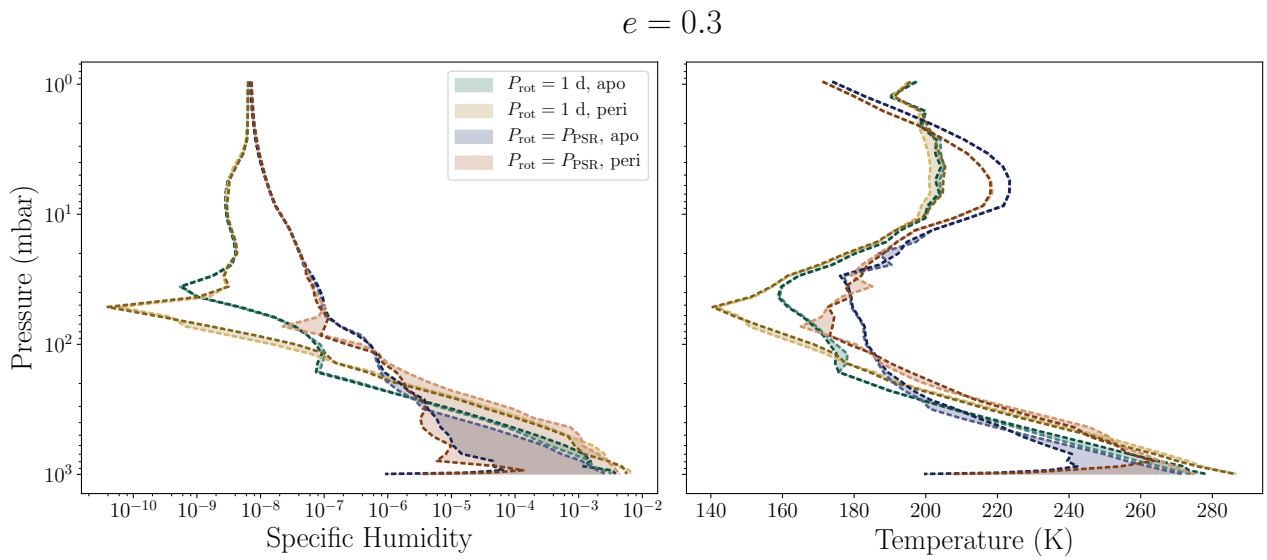


Figure 16. Same as Figure 5 for ocean depths of 10 meters, for $e = 0.3$.

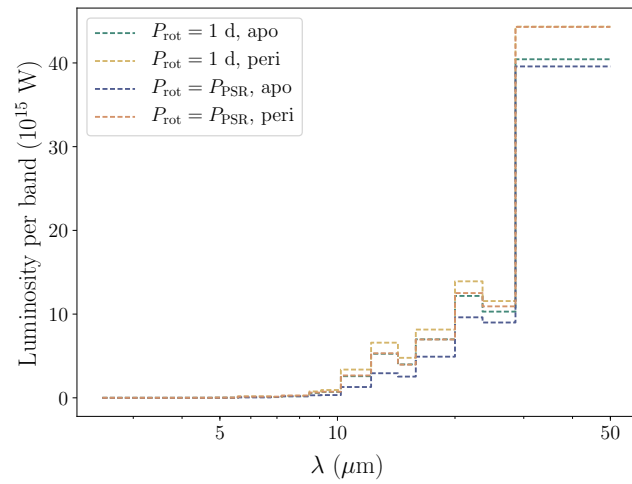
$e = 0.3$


Figure 17. Same as Figure 6 for ocean depths of 10 meters, for $e = 0.3$.

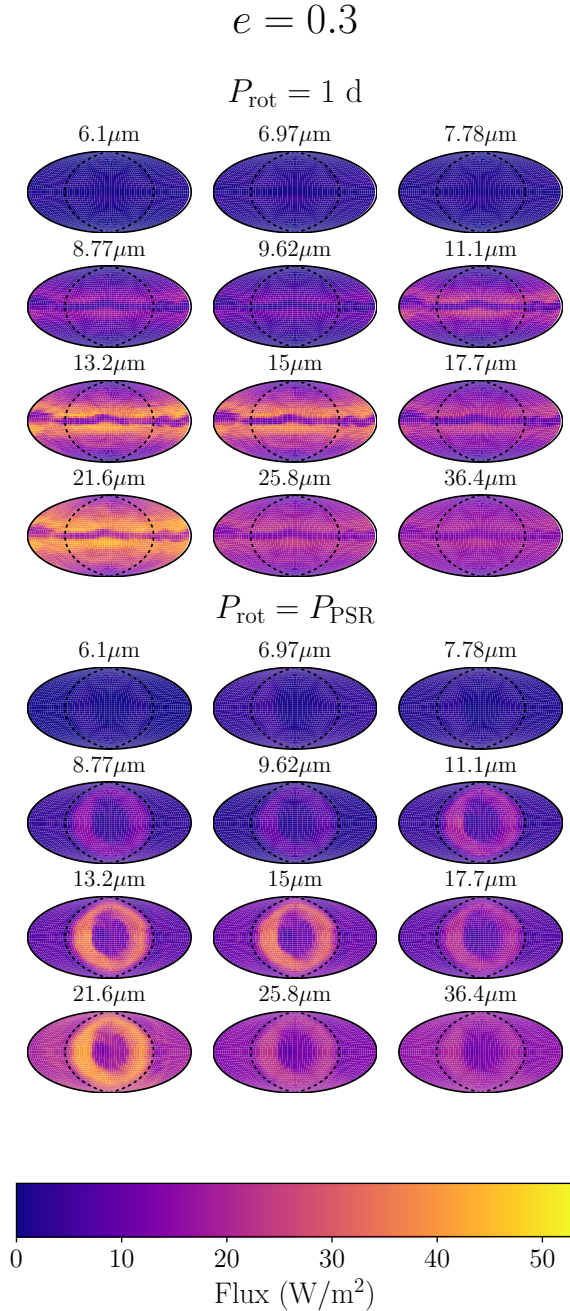


Figure 18. Same as Figure 7 for ocean depths of 10 meters, for $e = 0.3$.

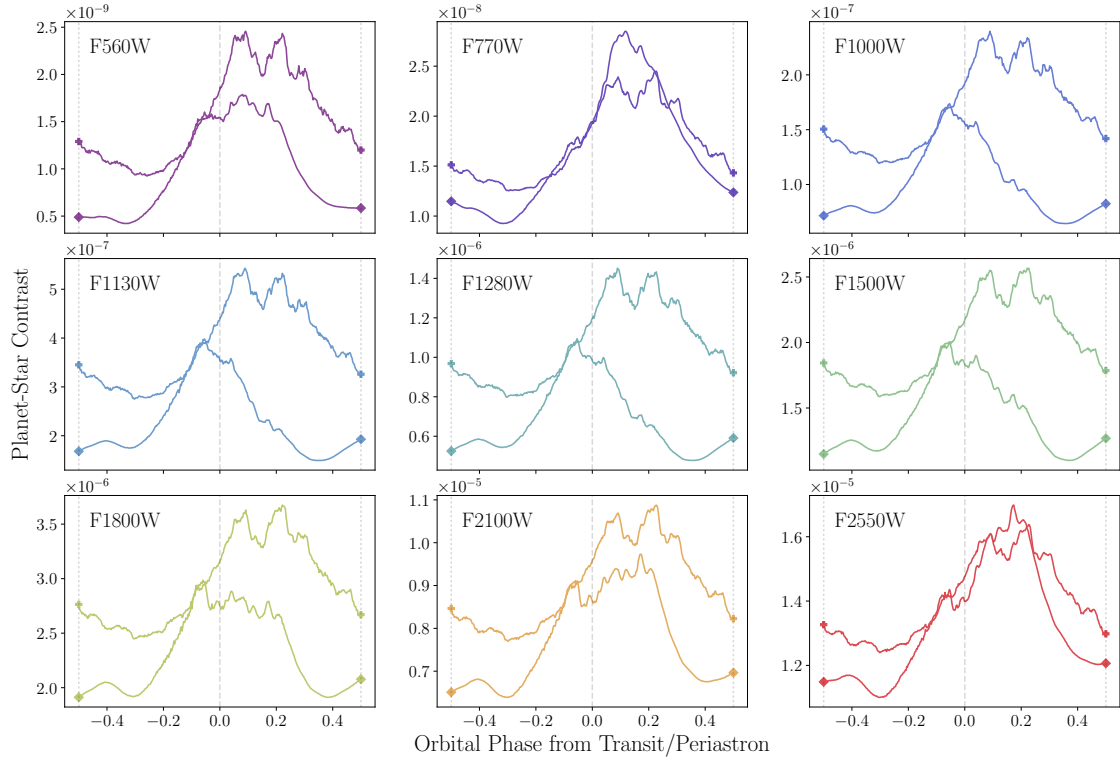
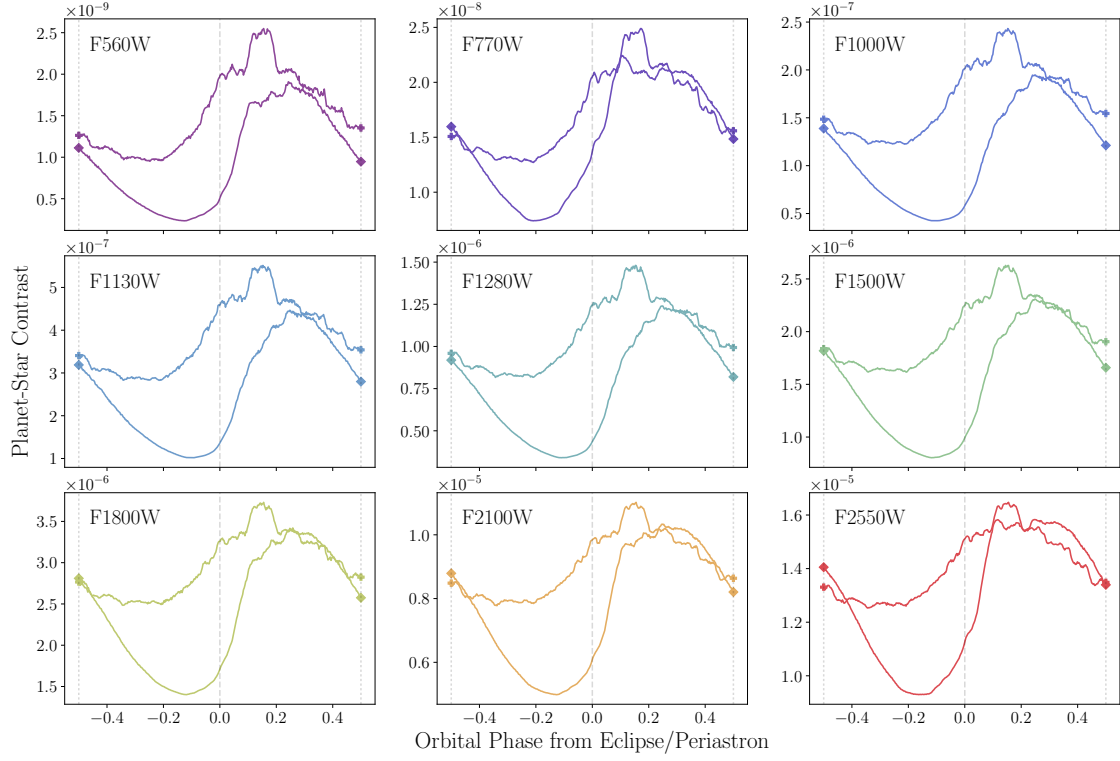
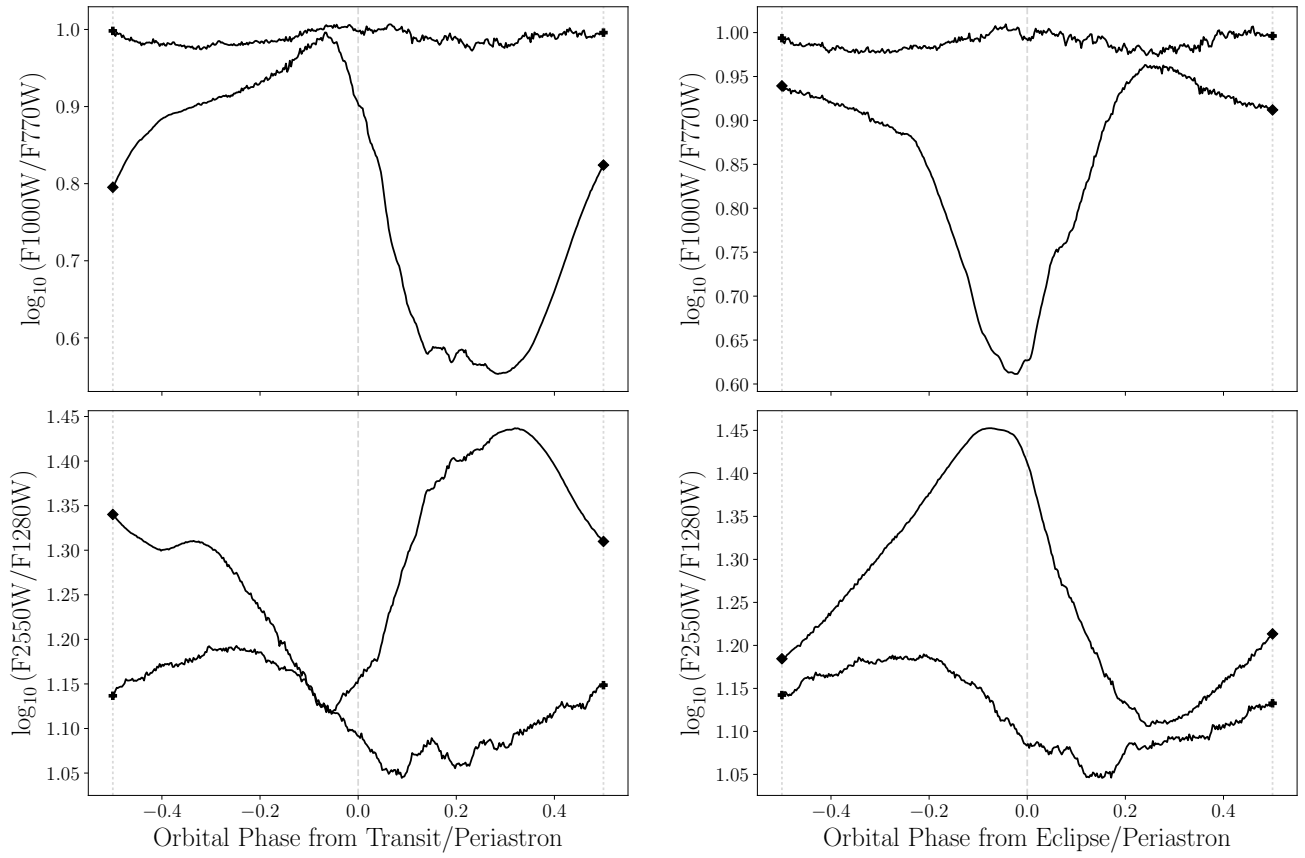
$e = 0.3, \omega = 90^\circ$

 $e = 0.3, \omega = 270^\circ$


Figure 19. Same as Figures 9–10 for ocean depths of 10 meters, for $e = 0.3$.

$e = 0.3, \omega = 90^\circ$ $e = 0.3, \omega = 270^\circ$ **Figure 20.** Same as Figures 11–12 for ocean depths of 10 meters, for $e = 0.3$.

$$e = 0.3$$

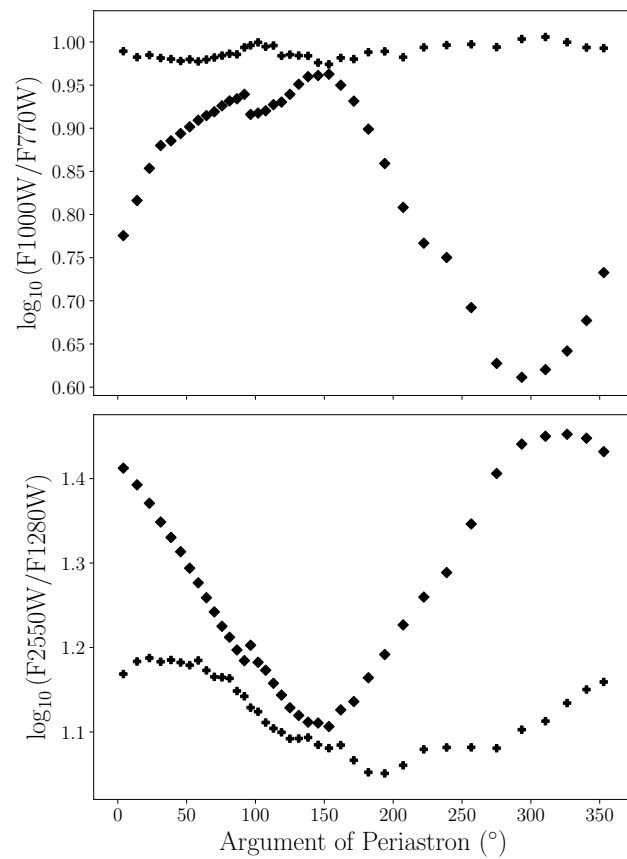


Figure 21. Same as Figure 13, $e = 0.3$, but for ocean depths at 10 meters.

REFERENCES

- Adams, A. D., & Kane, S. R. 2016, AJ, 152, 4
- Barnes, J. R., & Haberle, R. M. 1996, Journal of Atmospheric Sciences, 53, 3143
- Barnes, J. R., Haberle, R. M., Pollack, J. B., Lee, H., & Schaeffer, J. 1996, J. Geophys. Res., 101, 12753
- Barnes, J. R., Pollack, J. B., Haberle, R. M., et al. 1993, J. Geophys. Res., 98, 3125
- Barnes, R., Raymond, S. N., Jackson, B., & Greenberg, R. 2008, Astrobiology, 8, 557
- Bitz, C. M., Shell, K. M., Gent, P. R., et al. 2012, Journal of Climate, 25, 3053
- Bolmont, E., Libert, A.-S., Leconte, J., & Selsis, F. 2016, A&A, 591, A106
- de Wit, J., Lewis, N. K., Langton, J., et al. 2016, ApJL, 820, L33
- Dressing, C. D., Spiegel, D. S., Scharf, C. A., Menou, K., & Raymond, S. N. 2010, ApJ, 721, 1295
- Forget, F., Wordsworth, R., Millour, E., et al. 2013, Icarus, 222, 81
- Forget, F., Hourdin, F., Fournier, R., et al. 1999, J. Geophys. Res., 104, 24155
- Glasse, A., Rieke, G. H., Bauwens, E., et al. 2015, PASP, 127, 686
- Goldreich, P., & Soter, S. 1966, Icarus, 5, 375 . <http://www.sciencedirect.com/science/article/pii/0019103566900510>
- Haberle, R. M., Pollack, J. B., Barnes, J. R., et al. 1993, J. Geophys. Res., 98, 3093
- Hunke, E.C., L. W. 2008, CICE: The Los Alamos Sea Ice Model, Documentation and Software User's Manual, Version 4.0, Tech. Rep. LA-CC-06-012, Los Alamos National Laboratory, Los Alamos, New Mexico
- Hut, P. 1981, A&A, 99, 126
- Institute, S. T. S. 2017, JWST MIRI Filters and Dispersers, . <https://jwst-docs.stsci.edu/display/JTI/MIRI+Filters+and+Dispersers>
- Joshi, M. M., Haberle, R. M., & Reynolds, R. T. 1997, Icarus, 129, 450
- Kane, S. R., & Gelino, D. M. 2012, Astrobiology, 12, 940
- Kasting, J. F., Whitmire, D. P., & Reynolds, R. T. 1993, Icarus, 101, 108
- Kopparapu, R. K., Ramirez, R. M., SchottelKotte, J., et al. 2014, ApJL, 787, L29
- Kopparapu, R. k., Wolf, E. T., Arney, G., et al. 2017, ApJ, 845, 5
- Kopparapu, R. K., Ramirez, R., Kasting, J. F., et al. 2013, ApJ, 765, 131
- Kozai, Y. 1962, AJ, 67, 591
- Lebonnois, S., Hourdin, F., Eymet, V., et al. 2010, Journal of Geophysical Research (Planets), 115, E06006
- Lewis, N. K., Parmentier, V., Kataria, T., et al. 2017, ArXiv e-prints, arXiv:1706.00466
- Lidov, M. L. 1962, Planet. Space Sci., 9, 719
- Lin, S., & Rood, R. B. 1997, Quarterly Journal of the Royal Meteorological Society, 123, 2477
- Lin, S.-J., & Rood, R. B. 1996, Monthly Weather Review, 124, 2046
- Linsenmeier, M., Pascale, S., & Lucarini, V. 2015, Planet. Space Sci., 105, 43
- Merlis, T. M., & Schneider, T. 2010, Journal of Advances in Modeling Earth Systems, 2, 13
- Neale, R. B., et al. 2010, Description of the NCAR community atmosphere model (CAM 5.0), Tech. rep.
- O'Gorman, P. A., & Schneider, T. 2008, Journal of Climate, 21, 3815
- Rieke, G. H., Wright, G. S., Böker, T., et al. 2015, PASP, 127, 584
- Rossow, W. B. 1983, Journal of Atmospheric Sciences, 40, 273
- Salmon, R., & Held, I. 2001, 196
- Schneider, T. 2006, Annual Review of Earth and Planetary Sciences, 34, 655
- Shields, A. L., Barnes, R., Agol, E., et al. 2016, Astrobiology, 16, 443
- Shields, A. L., Bitz, C. M., Meadows, V. S., Joshi, M. M., & Robinson, T. D. 2014, ApJL, 785, L9
- Shields, A. L., Meadows, V. S., Bitz, C. M., et al. 2013, Astrobiology, 13, 715
- Showman, A. P., & Guillot, T. 2002, A&A, 385, 166
- Spiegel, D. S., Raymond, S. N., Dressing, C. D., Scharf, C. A., & Mitchell, J. L. 2010, ApJ, 721, 1308
- Wang, Y., Liu, Y., Tian, F., et al. 2016, ApJL, 823, L20
- Werner, M. W., Roellig, T. L., Low, F. J., et al. 2004, ApJS, 154, 1
- Williams, D. M., & Pollard, D. 2002, International Journal of Astrobiology, 1, 61

- Wolf, E. 2016, Extraterrestrial CAM, . .
<https://wiki.ucar.edu/display/etcam/>
Extraterrestrial+CAM
- Wolf, E. T., & Toon, O. B. 2013, Astrobiology, 13,
656
- . 2014, Geophys. Res. Lett., 41, 167
- . 2015, Journal of Geophysical Research
(Atmospheres), 120, 5775
- Wright, G. S., Wright, D., Goodson, G. B., et al.
2015, PASP, 127, 595
- Yang, J., Cowan, N. B., & Abbot, D. S. 2013,
ApJL, 771, L45
- Zalucha, A. M., Plumb, R. A., & Wilson, R. J.
2010, Journal of Atmospheric Sciences, 67, 673